8 New Insights into Ferroelectric Domain Imaging with Piezoresponse Force Microscopy

T. Jungk, Á. Hoffmann, and E. Soergel

Ferroelectric domain patterns are intensively investigated due to their increasing practical importance, e.g., for frequency conversion [1, 2] or high-density data storage [3]. For their characterization, a visualization technique with high lateral resolution is required. Among the wealth of techniques [4], piezoresponse force microscopy (PFM) has become a standard tool for visualizing micron-sized domain structures [5]. This is mainly due to its easy use without any specific sample preparation and the high lateral resolution of a few 10 nm. The vertical resolution of PFM reaches even the sub-picometer regime. Despite these impressive numbers, there are, however, only a few publications reporting quantitative data obtained with PFM. This seems to be amongst others due to a lack of knowledge on scanning force microscopy issues.

In this chapter we present an overview on PFM imaging restricted to the detection of ferroelectric domains on the polar faces of single crystals. We intend to provide a deeper insight into PFM imaging and thereby a more reliable interpretation of PFM images.

8.1 Introduction

We will start with a short survey on ferroelectricity to the extent it is necessary for further understanding of PFM imaging (Sect. 8.1.1). One of the most prominent examples for a ferroelectric crystal is lithium niobate ($LiNbO_3$), enabling very promising applications and thus being intensively investigated. We therefore briefly summarize the major properties of $LiNbO_3$ with regard to PFM (Sect. 8.1.2).

8.1.1 Ferroelectrics

From the 32 crystal classes ferroelectrics belong to the group of pyroelectrics, which represent a subgroup of the piezoelectric family [6]. Thus, ferroelectric crystals are piezo- and pyroelectric as well.

If stress is applied to a piezoelectric charges of different sign are generated on opposite crystal faces, which is called the direct piezoelectric effect. Due to thermodynamics, the inverse piezoelectric effect exists as well, which implies that the crystal deforms when an electrical field is applied to it. A subgroup of the piezoelectrics is the pyroelectric crystal class that includes 10 members (1, 2, 3, 4, 6, m, mm2, 3m, 4mm, 6mm). Even without an external electrical field or mechanical stress, these crystals exhibit a spontaneous polarization P_S due to a dislocation of the positive and negative ions in the crystal lattice. A change of the temperature causes a deformation of the crystal along its polar axis and vice versa, which is called the pyroelectric effect.

Several members of the pyroelectric crystal class show a reversible spontaneous polarization with two or more stable states that can be reached via an external electrical field or via mechanical stress. A spatial region with a homogeneous polarization is called ferroelectric domain. Ferroelectric domains only exist in well-defined crystallographic orientations [7], such as 180° domains along a polar axis. Moreover, the relation between polarization and applied electrical field is given by a hysteresis loop. In contrary to piezo- and pyroelectricity, the ferroelectric crystals cannot be predicted by symmetry considerations but have to be discovered experimentally. A detailed description of ferroelectricity can be found in the literature [8–10].

8.1.2 Lithium Niobate ($LiNbO_3$)

In its ferroelectric phase, $LiNbO_3$ belongs to the point group 3m, i.e., it is a uniaxial crystal with a 3-fold rotation symmetry. The orientation of the crystallographic c-axis, which is defined as z-axis in Cartesian coordinates, is given by the position of the cations Li^+ and Nb^{5+} relative to the position of the oxygen anions [11]. The domain formation is based on displacement polarization along the z-axis, thus antiparallel 180° domains develop. We primarily utilized congruently melting $LiNbO_3$ produced by the Czochralski method [12], which was prepared in the desired domain configuration by electrical field poling. Quite often we investigated periodically poled lithium niobate (PPLN).

If the crystal is poled from one domain orientation into the other, all crystal properties described by odd rank tensors have to switch sign, such as the piezoelectric tensor which is the basis for PFM. In the case of $LiNbO_3$, the application of the von Neumann principle to the point group 3m gives 4 independent components (d_{113}, d_{222}, d_{311}, and d_{333}) for the piezoelectrical tensor. Note that the longitudinal piezoelectrical effect described by the diagonal tensor elements d_{iii} is independent of the crystal thickness. An exact mathematical description of the piezoelectrical effect can be found in [13].

For stoichiometric $LiNbO_3$, several material parameters change [14], as it is the case for doped $LiNbO_3$ too [15]. A detailed summary of the properties of $LiNbO_3$ can be found in [16].

8.2 Principles of Scanning Force Microscopy (SFM)

The main attention in this section is focussed on a sound understanding of PFM investigation of single crystals. Therefore a deeper insight into scanning force microscopy (SFM) in general is required. In most PFM publications a detailed description of SFM is missed out, that is why we will pay special attention to this topic. After reviewing the tip-surface interactions relevant for the investigation of ferroelectric crystals (Sect. 8.2.1), we will describe the resulting responses of the cantilever (Sect. 8.2.2). A separate section is dedicated to the problem of cross-talk between different cantilever movements (Sect. 8.2.3). This issue is of major importance as cross-talk can give rise to pretended signals bereft of any physical origin. Finally, special attention is payed to the calibration of the SFM with regard to PFM applications, since an accurate calibration is mandatory to allow quantitative measurements (Sect. 8.2.4).

In the following, we assume a standard commercial scanning force microscope equipped with a laser-beam deflection readout [17]. The microscope is operated in contact mode. Furthermore an electrical connection allowing the application of moderate voltages to the tip is provided.

8.2.1 Tip-Cantilever-Surface Interactions

Mechanical Parameters of the Tip and Cantilever

The dimensions of a typical commercially available SFM probe used for PFM are the following: cantilever width $w = 25$–$35\,\mu\text{m}$, cantilever length $l = 100$–$300\,\mu\text{m}$, tip height $h \approx 15\,\mu\text{m}$, and tip radius $r \approx 50\,\text{nm}$ (Fig. 8.1). As it is obvious from these dimensions, the lateral resolution is dominated by the apex of the tip. Any additional contribution of the cantilever can only resolve features of the size of the

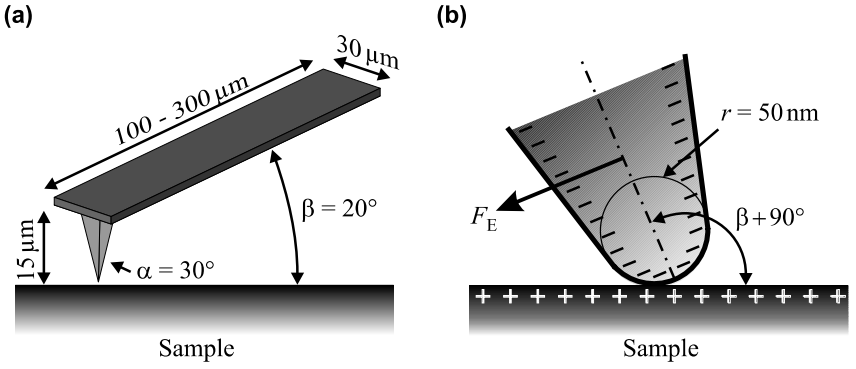

Fig. 8.1. (**a**) Typical dimensions of a commercially available cantilever and tip. (**b**) Closer view to the conical apex of the tip from which the tip radius r is defined. Possible electrostatic forces F_E due to an inclination angle β are depicted

cantilever itself. Thus, in the case of the visualization of µm-sized structures, the cantilever has no impact on the imaging process.

Electrostatic Interaction between Tip & Cantilever and Surface

Since the spontaneous polarization P_s leads to a surface charging, the electrostatic interaction between tip & cantilever and the surface are of major interest. Again an interaction between the cantilever and the surface cannot account for any SFM imaging with a lateral resolution better than the cantilever size. Because the tip is in contact with the surface, electrostatic forces, although present, cannot result in a vertical displacement of the tip. Note that for electrostatic force microscopy [18], the SFM is operated in noncontact mode, so the situation is completely different. One might think that due to the inclined position of the tip with respect to the surface, the asymmetric field distribution could lead to a torsion (Fig. 8.1(b)). However, a rough estimate of the torsional moment excludes such a contribution. Furthermore, we performed a series of experiments investigating the PFM contrast on PPLN samples for different inclination angles β ranging from 0° to 60° by mounting the sample on different wedges. Indeed, the contrast was observed to be independent of the angle β.[1]

8.2.2 Cantilever Movements

Depending on the relative orientation of the driving force with respect to the axis of the cantilever, the latter can perform three mostly independent movements: (i) deflection if the force acts along the tip axis, (ii) torsion if the force acts perpendicular to the tip and to the cantilever, and (iii) buckling if the force acts perpendicular to the tip but along the cantilever (Fig. 8.2). Whereas deflection and torsion can be found in every standard textbook [17], buckling is not that much known, that is why a more detailed description seems appropriate.

Firstly, it is important to note that a buckling of the cantilever gives rise to a signal in the vertical channel and can thus not be easily distinguished from a deflection of the cantilever. From the side view in Fig. 8.2(c) it can be seen that the readout of buckling is very sensitive to the position of the laser beam on the back side of the cantilever: displacing the laser beam from the very end on top of the tip towards the middle of the cantilever results in an inversion of the readout signal. Thus, it is evident that buckling cannot be observed if the laser spot is too large, but also an inappropriate adjustment of the laser spot on top of the anti-node can discard the buckling signal.

[1] These statements are not in contradiction to the lateral signal explained later via electrostatic forces. Here we discuss an electrostatic contribution to the PFM signal on domain faces, i.e., the surface underneath the tip is homogeneously charged. In the case of lateral forces, however, the signals occur only at the domain boundaries and thus at the places where an electric field in plane with the surface is present.

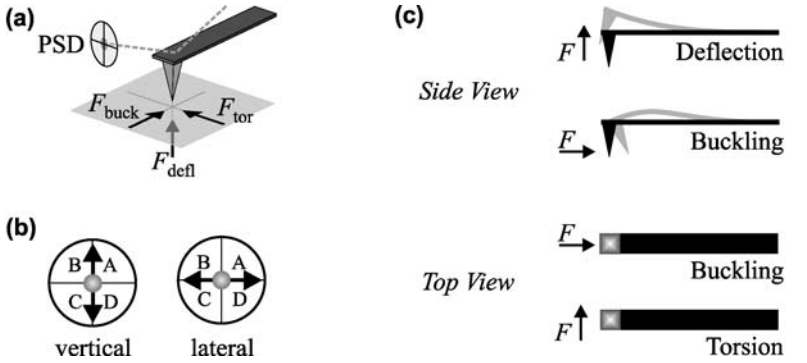

Fig. 8.2. Forces acting on the tip with the resulting movements of the cantilever (**a**, **c**). In (**b**) the definition of the readout channels of the position sensitive detector (PSD) is given

It is also worth to note that the deflection signal measures a height displacement of the tip (in m), whereas both torsion and buckling measure a force acting on the tip (in N). A detailed calibration procedure for SFM will be given below (Sect. 8.2.4).

8.2.3 Cross-Talk

Although often ignored, cross-talk between the vertical and the lateral readout channel is a serious source for erroneous signals. Whereas electronic cross-talk (due to an imperfect electric shielding) and mechanical cross-talk (primarily arising only on samples with pronounced topography) can in general not be influenced by the user, the cross-talk originating from a misalignment of the optical detection system can be eliminated by a simple electronic circuit [19]. This cross-talk arises if the segmented photodetector is rotated with respect to the plane of the readout laser beam. Depending on the specific SFM, the mounting of the cantilever and thus the subsequent laser-beam adjustment, the cross-talk between the vertical and the lateral channel can amount up to 30%. A pure deflection of the cantilever thus leads to a pretended torsional signal, bereft of any physical origin.

To obtain reliable data it is mandatory to compensate for the cross-talk. The amount of cross-talk, and thus the necessity to compensate for it, can be estimated in a very simple way: put the tip far away from the surface and excite the cantilever to vibrate at the first deflection mode, the "standard" resonance frequency. Any signal in the lateral readout channel must originate from cross-talk, since the torsional vibration modes have a much higher resonance frequency [20].

8.2.4 Calibration

Usually, the calibration of the SFM for PFM measurements is performed using an α-quartz sample as calibration standard as, e.g., described in [21]. However, due to the system-inherent background (Sect. 8.4), that calibration procedure fails. This is

described in detail elsewhere [22]. Instead, the calibration should be performed with a piezoelectric sample exhibiting a large piezoelectric coefficient; even if the latter is not known with high accuracy, it can easily be determined within the calibration procedure. For example, a lead zirconate titanate (PZT) disc is well suited. In brief, for a reliable calibration of the SFM and especially for PFM applications, three steps have to be accomplished:

- Calibration of the z-scanner of the SFM.
- Measurement of thickness change Δt_{PZT} of the calibration sample for a specific voltage U_{tip}. This measurement is performed with the so-called height-mode of the SFM. That is why the piezoelectric constant of the calibration sample has to be large in order to yield measurable thickness changes Δt at moderate voltages.
- Read-out of the output of the lock-in amplifier P_{PZT} while disabling the feedback-loop of the SFM (with the same sample and otherwise unchanged settings as used in the step before).

This procedure allows to determine the calibration constant $k = \Delta t_{\mathrm{PZT}}/P_{\mathrm{PZT}}$, which can then be used to measure any other material.

8.3 Principles of Piezoresponse Force Microscopy (PFM)

The aim of PFM measurements is to detect a deformation of the sample due to the converse piezoelectric effect. Therefore an alternating voltage U_{tip} is applied to the tip and the response, i.e., the thickness change Δt of the sample due to the converse piezoelectric effect is measured via lock-in detection. Although straightforward at first sight, PFM measurements gave rise to a wealth of discussions mainly due to their strong frequency dependence [23, 24] which lead to alternative explanations of the origin of the domain contrast [25–27]. Above all, another name was introduced for one and the same method – dynamic contact electrostatic force microscopy [25].

Within this section, our aim is to recall the generally used setup and standard settings for PFM measurements in order to specify them in a closed form (Sect. 8.3.1). We will then present an analysis of PFM measurements taking into account the system-inherent background (Sect. 8.3.2) followed by its vectorial description (Sect. 8.3.3).

8.3.1 PFM Setup & Standard Settings

To utilize an SFM for piezoresponse force microscopy requires mainly two instrumental features: (i) an electrical connection to the tip and (ii) direct access to the signals of the position sensitive detector recording the movement of the cantilever. Furthermore, a lock-in amplifier is necessary for sensitive readout of the cantilever movement. Figure 8.3 shows the standard setup for PFM. In the following, the crucial parts of the experimental setup are described in order to define the parameters and denotations used further on. In addition, our experimental settings for PFM operation are given:

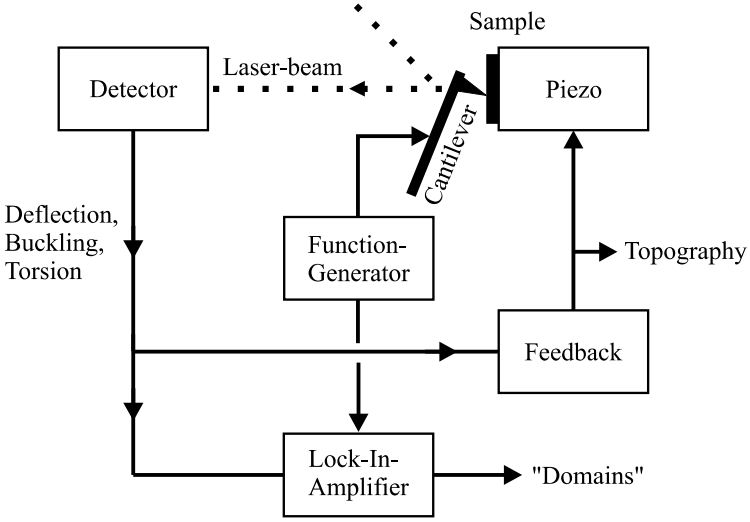

Fig. 8.3. Setup for PFM measurements

- Tip of the SFM: for PFM operation, the tip must be conductive and electrically connected to allow the application of voltages. The resonance frequency of the cantilever is not crucial; it should always be far away from the frequency of the alternating voltage applied to the tip. Typically, cantilevers with resonance frequencies $f_0 > 100\,\mathrm{kHz}$ are utilized. The alternating voltage applied to the tip is usually chosen to have a frequency between 10 kHz and 100 kHz with an amplitude $U \leq 20\,\mathrm{V_{pp}}$. The time constant of the feedback-loop of the SFM must be large compared to the period of modulation of the applied voltage to avoid a compensation of the signal.
  We mostly utilize Ti–Pt coated tips (MicroMasch) with resonance frequencies $f_0 = 150$–$400\,\mathrm{kHz}$, spring constants $k = 3$–$70\,\mathrm{N/m}$ and apply an alternating voltage of 30–60 kHz with an amplitude of $\sim 10\,\mathrm{V_{pp}}$.
- Sample: in large part, PFM measurements are performed with crystals exhibiting antiparallel domains only. For investigation, the samples are cut in such a way that the domain boundaries are perpendicular to the surface to be studied. We will restrict ourselves to such a configuration exclusively.
- SFM: generally all scanning force microscopes are suited for PFM operation as long as they allow application of voltages to the tip and separate readout of the cantilever movement. The scanning velocity has to be adapted to the rise time of the lock-in amplifier.
  We use a SMENA SFM (NT-MDT) modified to apply voltages to the tip and upgraded with an additional interface board for readout of the cantilever movement. Typical scanning velocity is about 1 µm/s.
- Lock-in amplifier: most PFM setups use dual-phase lock-in amplifiers which allow to chose between two output schemes: (i) in-phase output (also denoted as

X-output) and orthogonal output (Y-output) or (ii) magnitude $R = \sqrt{X^2 + Y^2}$ and phase $\theta = \arctan(Y/X)$. These output signals of the lock-in amplifier will be named PFM signals: **P** on a positive $+z$ domain face and **N** on a negative $-z$ domain face. To specify the output (and thus the component of the particular vector), the adequate symbol (X, Y, R, or θ) will be added as a subscript. For example, P_X denotes the in-phase output signal of the lock-in amplifier on a positive $+z$ domain face.

The experiments presented here are performed with a SR830 lock-in amplifier (Stanford Research Systems). Typical settings are 1 mV for the sensitivity and 1 ms for the time constant.

8.3.2 System-Inherent Background in PFM Measurements

According to the physical principles of the converse piezoelectric effect, PFM signals have to meet the following requirements:

- Depending on the orientation of the polar axis, the piezoresponse must be either in phase or out of phase by 180° with respect to the alternating voltage applied to the tip.
- The amplitude of the PFM signal must be same on $+z$ and $-z$ domain faces.
- No frequency dependence of the PFM signals is expected. This holds true for frequencies < 100 kHz as piezomechanical resonances usually occur at much higher frequencies [28].

Interestingly, these physically mandatory properties for PFM signals are not generally fulfilled [23, 24, 29–33]. That is why a series of alternative explanations [25–27] or at least additional contributions to the PFM signal [34, 35] have been discussed. However, an accurate analysis of the situation reveals the presence of a system-inherent background, strongly affecting the measurements [36, 37]. As a consequence, the PFM signals turn out to be a superposition of the background signal **B** and the piezoresponse signal **d** of the sample.

To prove the existence of the system-inherent background, we performed comparative measurements on PPLN samples and on standard microscope glass slides, the latter being not piezoelectric. We firstly determined the frequency dependence on the $+z$ and $-z$ faces thus recording P_X and N_X. Due to the requirements listed above, the sum of those two signals must be free of any piezoelectric contribution. The result, however, can be seen in Fig. 8.4(a), where we plotted $\frac{1}{2}(P_\mathrm{X} + N_\mathrm{X})$. As pronounced frequency dependence is present, however, the origin of this signal must be independent of the piezoelectric properties of the sample. This was demonstrated by comparative measurements on a microscope glass slide, showing the same frequency dependence (Fig. 8.4(b)). The small difference of both scans is shown in Fig. 8.4(c), the vertical scale being expanded by a factor of ten.

8.3.3 Vectorial Description

In order to clarify the statements about the system-inherent background presented above, we show a vector diagram illustrating the case for two different frequencies

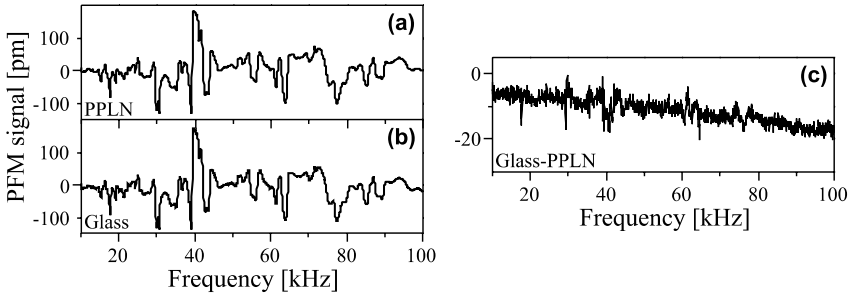

Fig. 8.4. Frequency dependence of the in-phase PFM background signal on a PPLN surface (**a**), on a glass surface (**b**), and their difference (**c**)

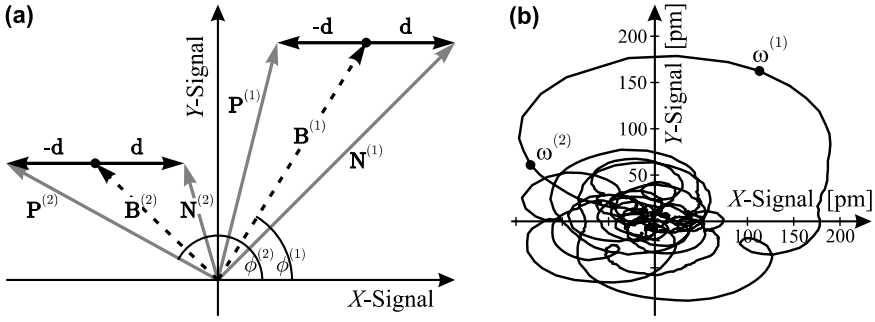

Fig. 8.5. (**a**) Vector diagram showing the PFM signals on the $\pm z$ domain faces of a ferroelectric sample (X and Y: in-phase and orthogonal output of the lock-in amplifier) for two different frequencies $\omega^{(1)}$ and $\omega^{(2)}$. The superscripts indicate the corresponding signals: the PFM signal **P** (**N**) measured on a $+z$ ($-z$) domain, the background **B**, and its corresponding phase ϕ. The piezoresponse signal from a $\pm z$ domain face is denoted by $\mp\mathbf{d}$. (**b**) Frequency dependence (10–100 kHz) of the background **B** determined on a PPLN surface with 10 V applied to the tip

$\omega^{(1)}$ and $\omega^{(2)}$ of the alternating voltage applied to the tip (Fig. 8.5(a)). At a specific frequency $\omega^{(1)}$, a background PFM signal $\mathbf{B}^{(1)}$ is present. The piezoresponse of the sample contributes **d** for the $-z$ face and $-\mathbf{d}$ for the $+z$ face to the PFM signal, both of same amplitude with a 180° phase shift in between. This results in the measurement of $\mathbf{N}^{(1)} = \mathbf{B}^{(1)} + \mathbf{d}$ for the $-z$ face and $\mathbf{P}^{(1)} = \mathbf{B}^{(1)} - \mathbf{d}$ for the $+z$ face. It is important to note that the phasing between $\mathbf{P}^{(1)}$ and $\mathbf{N}^{(1)}$ is not 180° and that their amplitudes are unequal and larger than expected. The same considerations apply for any other frequency $\omega^{(2)}$. It is obvious from Fig. 8.5(a) that although **d** is unchanged for both frequencies, the PFM signals measured at different frequencies differ with respect to amplitude and phase. This can be verified experimentally with an oscilloscope in X–Y-display mode when applying different frequencies of the alternating voltage to the tip while scanning across a domain wall.

To underline the arbitrariness of the background Fig. 8.5(b) shows an X–Y-diagram of its frequency dependence from 10 kHz to 100 kHz. Note that the big slope covers a frequency span from 39 kHz to 42 kHz only.

8.4 Consequences of the System-Inherent Background

The origin of the system-inherent background is not clear until now, and therefore getting rid of it seems quite difficult. In general one can assume, however, that the whole SFM head acts as a mechanical resonance box. Therefore minimum changes like the readjustment of the optical readout changes the frequency spectrum. Also the elongation of the tube scanner was found to have an impact on the background. The background shows the very same linear dependence on the applied voltage as the piezoresponse signal. Thus, a separation of the two signals via a tricky choice of the applied voltage fails. A main reason for renouncing to invest into a efficient suppression of the background is its amplitude: typical values are several 10 pm/V (similar to piezoelectric coefficients of many ferroelectric crystals). The high sensitivity of the lock-in amplifier makes these vibrations easily accessible, however, suppressing a complex mechanical setup from oscillating with such small amplitudes is not quite realistic. Of course the investigation of ceramics such as PZT with much larger piezoelectric coefficients [38] is only marginally influenced by the system-inherent background.

In this section we want to point out the strong influences of the background on the PFM measurements (Sect. 8.4.1). We also give a – fortunately very easy – solution for background-free PFM imaging (Sect. 8.4.2).

8.4.1 Background-Induced Misinterpretations

Several surprising features concerning the domain contrast as well as the shape and location of domain boundaries turn out to possibly originate from the system-inherent background [37]. Of course, also physical effects can influence the domain contrast and the domain boundaries, however, a careful analysis of the measured data is mandatory to avoid misinterpretation. In the following, we exemplify possible consequences of the background:

- Enhancement of the domain contrast;
- Nulling of the domain contrast;
- Inversion of the domain contrast;
- Arbitrary phase difference between $\pm z$ domains;
- Shift of the domain boundary;
- Change of the shape of the domain boundary.

Detailed considerations based on the vector diagram of Fig. 8.5(a) allow one to understand the influence of the background on the domain contrast and the phase

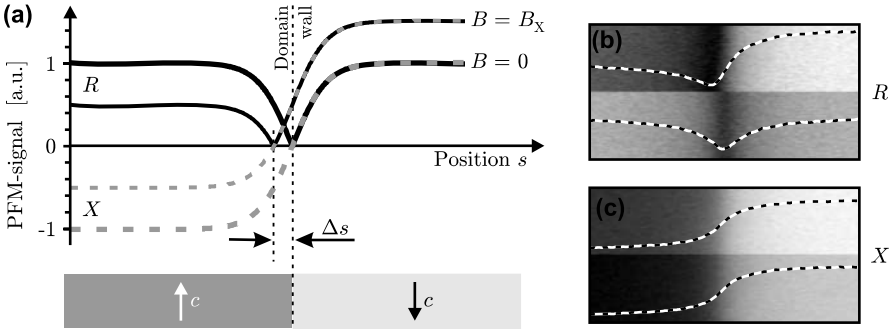

Fig. 8.6. Influence of the read-out settings of the lock-in amplifier on the detected domain wall. (**a**) Model predictions of the expected PFM signals, where *black lines* correspond to the R-signal and *grey dashed lines* to the X-signal without ($B = 0$) and with the presence of a background signal ($B = B_X$). The model is confirmed by PFM measurements of a single domain boundary in $LiNbO_3$. During image acquisition, the frequency of the applied voltage was changed, thereby adding a background signal B_X. Using the R-output leads to a pretended shift of the domain boundary (**b**), whereas the PFM image recorded with the X-output just becomes brighter (**c**). The line scans are averages over 20 image lines. The image size is $1 \times 0.5\,\mu m^2$

signal of the lock-in amplifier. The consequences of the background signal on the shape and location of the domain boundaries in PFM measurements when using the magnitude output of the lock-in amplifier, however, need a more careful analysis. In order to clearly expose the contributions of the background to the PFM signal, it is reasonable to discuss two special cases separately: the phasing between background and piezoresponse signal being (i) 0° or 180° and (ii) 90° or 270°. In (i) the background lies on the X-axis in Fig. 8.5(a) and in (ii) parallel to the Y-axis. In general the phasing will be arbitrary leading to a superposition of the phenomena described in the following.

Background B along X

The consequences of a background along the X-axis can be seen in Fig. 8.6(a), where scan lines across a domain boundary for both the X- and R-outputs of the lock-in amplifier are simulated. In the case of no background signal ($B = 0$, thick lines), both readout signals show the domain boundary at its real position $s = 0$, in the R-signal as a minimum and in the X-signal as the inflection point of the slope. When adding the background B_X, the minimum of the R-signal is shifted by Δs pretending the domain boundary to be at a different location. Moreover, a distinct change of the domain contrast can be observed. Figures 8.6(b, c) show images of a single domain boundary recorded simultaneously with the X- and R-outputs of the lock-in amplifier. After the first half of the image, the frequency of the alternating voltage is changed in order to alter the background. Whereas in the X-signal the location of the domain boundary is not affected (Fig. 8.6(c)), the image taken with

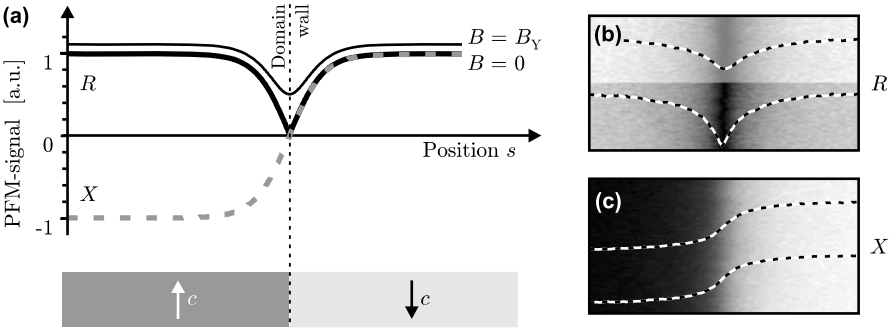

Fig. 8.7. Influence of the read-out settings of the lock-in amplifier on the detected domain boundary. (**a**) Model predictions of the expected PFM signals, where *black lines* correspond to the R-output and *grey dashed lines* to the X-output. The model is confirmed by PFM measurements of a single domain boundary in $LiNbO_3$. During image acquisition, the frequency of the voltage applied to the tip was changed, thereby adding a background B_Y. Using the R-output leads to a pretended broadening of the domain boundary (**b**), whereas the image of the X-output stays unchanged (**c**). The line scans are averages over 20 image lines. The image size is $1 \times 0.5\,\mu m^2$

the R-output shows a distinct shift of the domain boundary (Fig. 8.6(b)). As a further consequence of the in-phase background, a broadening and also an asymmetry of the detected domain wall is pretended.

Background B along Y

The situation for a background along Y can be explained in a similar way. As can be seen from Fig. 8.7(a), PFM images recorded with the R-output show the domain boundaries only. Their full width at half maximum W broadens with increasing background. At the same time, the contrast of the domain boundary decreases. Figures 8.7(b,c) show PFM images of a single domain boundary recorded simultaneously with the X- and R-outputs of the lock-in amplifier. After recording half of the image, the frequency of the alternating voltage is changed in order to alter the background. Whereas in the X-signal no changes can be observed (Fig. 8.7(c)), the image taken with the R-output shows a distinct broadening of the domain wall as well as a faded contrast (Fig. 8.7(b)).

8.4.2 Background-Free PFM Imaging

As can be seen from the Figs. 8.6 and 8.7, reliable experimental data in PFM imaging can be obtained when using the X-output of the lock-in amplifier for data acquisition.

From the experimental side, however, there is an additional problem arising: although the piezoelectric response must be in-phase with the alternating voltage applied to the tip (at least for frequencies $<100\,kHz$), there is always a small phase

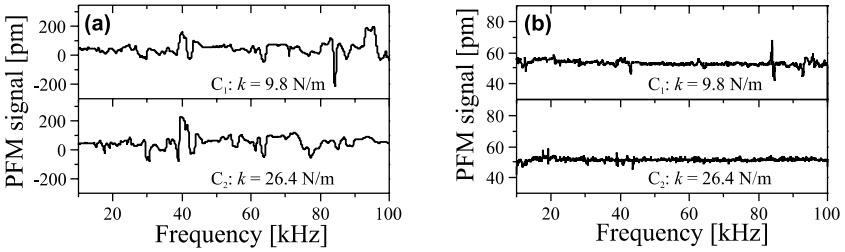

Fig. 8.8. Frequency spectrum on a $-z$ domain face of $LiNbO_3$ before (**a**) and after (**b**) background subtraction for two different cantilevers (C_1 and C_2) with a voltage of 10 V_{pp} applied to the tip

shift ($<10°$) originating from the read-out electronics. In the vector diagram of Fig. 8.5(a), the piezoresponse signal **d** would show up slightly tilted. To extract nevertheless correct data from PFM measurements, the easiest solution is to set the phase of the lock-in amplifier such that no domain contrast is visible in the Y-output of the lock-in amplifier. This corresponds to a rotation of the vector diagram in the coordinate system in Fig. 8.5(a). An equivalent (and even more precise) solution is a rotation of the coordinate system after image acquisition such that the standard deviation of the of the image recorded with the Y-output is minimized.

8.5 Quantitative Piezoresponse Force Microscopy

With the basic knowledge acquired above and having performed a reliable calibration of the microscope, it is now possible to record quantitative data for the PFM amplitude (Sect. 8.5.1) and the domain wall width seen by PFM (Sect. 8.5.2).

8.5.1 Amplitude of the PFM Signal

To obtain quantitative data of the piezoelectric deformation of the sample underneath the tip, the PFM background must be corrected. The background can be determined with the help of a PPLN crystal, measuring the piezoresponse on both domain faces (P_X and N_X) and then calculating $B = \frac{1}{2}(P_X + N_X)$. Another way to determine B consists in using a nonpiezoelectric sample (glass, metallized surface) as a reference. Figure 8.8(a) shows the uncorrected PFM signal and (b) the result after background correction for a frequency scan from 10 kHz to 100 kHz. The amplitude of the PFM signal becomes frequency independent, as it is required from the physics of the converse piezoelectric effect in this frequency regime. Furthermore, the obtained value for the piezoelectric coefficient of $\sim$6 pm/V is in first order consistent with other measurements. Interestingly, for this value, the agreement is not very good in literature, the published data varying between 6 pm/V and 23 pm/V (e.g., see references within [39]).

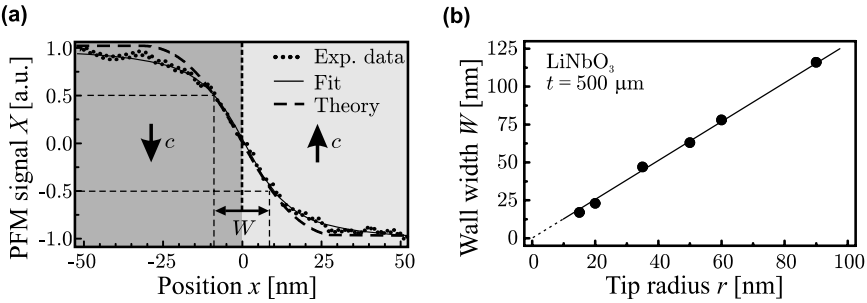

Fig. 8.9. (**a**) Measured PFM signal line scan (•) across a 180° domain wall in $LiNbO_3$ recorded with a tip of $r = 15\,\text{nm}$ radius. The domain wall width W is determined fitting the data using (8.1). For comparison, a line scan is shown that was calculated with the theoretical model for a tip of the same radius. (**b**) Measured domain wall width W as a function of the nominal tip radius r. The straight line was calculated using an analytical model

One explanation for obtaining such small values with PFM lies in the strongly inhomogeneous electric field of the tip inside the crystal. We therefore performed comparative measurements with single crystals exploring two different configurations [39]: (i) standard PFM with the tip acting as top-electrode and (ii) large-area electrode via metallization of the top face of the crystal. We have found that for the case (ii) with a homogeneous electric field inside the crystal, the measured value was larger by roughly a factor of three, i.e., 20 pm/V. In order to sustain this result, we performed comparative measurements with α-quartz and $KTiOPO_4$ [40]. All samples exhibited the same reduction of the signal by a factor of three using standard PFM. Obviously the strong restriction of the electric field within a few μm^3 leads to clamping inside the crystal thus limiting the deformation to roughly 1/3 of the expected value. Hence, PFM is not suited to yield reliable piezoelectrical coefficients [22].

8.5.2 Domain Wall Width

With the correction of the system-inherent background, the lateral resolution of PFM can reliably be answered. As a measure of the wall width seen by PFM (not to be confused with the real wall width which is expected to be few lattice units [41]), we determined the full width at half maximum W of the slope of the PFM signal across a domain boundary. Figure 8.9(a) shows an example for a measurement performed on $LiNbO_3$ using a tip with a radius of $r = 15\,\text{nm}$ only. We then fitted the curve with

$$X(x) = A \tanh\left(\frac{x}{w}\right) + B \arctan\left(\frac{x}{w}\right) \tag{8.1}$$

to determine W. In addition the graph also shows the theoretical curve calculated with a simple analytical model. A detailed description, however, would go beyond the scope of this contribution and can be found elsewhere [42]. Note that

Table 8.1. Domain wall width W measured for different samples with tips of radius r. c-$LiNbO_3$: congruently melting and s-$LiNbO_3$: stoichiometric lithium niobate respectively

Sample	Domain wall width W [nm]		Dielectric anisotropy
	$r = 15\,\text{nm}$	$r = 35\,\text{nm}$	$\gamma = \sqrt{\varepsilon_z/\varepsilon_r}$
$BaTiO_3$	19	46	0.17
$KNbO_3$	18	45	0.34
$KTiOPO_4$	17	46	1.16
c-$LiNbO_3$	17	46	0.58
s-$LiNbO_3$	17	45	0.58
Mg:$LiNbO_3$	18	47	0.58
$LiTaO_3$	18	45	1.10
$Sr_{0.61}Ba_{0.39}Nb_2O_6$	18	48	1.52
$Pb_5Ge_3O_{11}$	18	45	1.40

$W = 17\,\text{nm}$ is the so far highest lateral resolution achieved with PFM in bulk single crystals.

In order to establish a relation between tip radius r and lateral resolution, we determined W for a series of tips with different tip radii. The result depicted in Fig. 8.9(b) shows a clear linear dependence, which is consistent with an infinite sharp domain boundary.

We also compared W for different crystals using two tips of different radius. All samples show the same width W for a specific tip of radius $r = 15\,\text{nm}$ or $r = 35\,\text{nm}$ within an error of $\pm 1\,\text{nm}$, although their dielectric anisotropy $\gamma = \sqrt{\varepsilon_z/\varepsilon_r}$ differ as listed in Table 8.1. A detailed calculation of the electric field distribution inside the crystal shows, however, that the latter is independent of γ, thus although the amplitude of the PFM signal differs, the slope of W has to be same for all crystals [42].

8.6 Ferroelectric Domain Imaging by Lateral Force Microscopy

The contrast mechanism for the detection of ferroelectric domain boundaries with lateral force microscopy was generally assumed to be caused by the deformation of the sample at the domain boundaries due to the converse piezoelectric effect [43, 44]. The tip was expected to be deflected sidewise due to the slope of the surface. In this case, however, the amplitude of the lateral signal should scale with the load of the tip. This was not observed [45]. A quantitative analysis of the measured forces shows that the electrostatic interaction between the charged tip and the electric fields arising from the surface polarization charges causes the contrast (Sect. 8.6.1). We therefore call the detection technique lateral electrostatic force microscopy (LEFM). Ferroelectric domain structures in a single crystal turned out to be an ideal sample to show the different movements of the cantilever (deflection, torsion, buckling) without additional topographic features (Sect. 8.6.2).

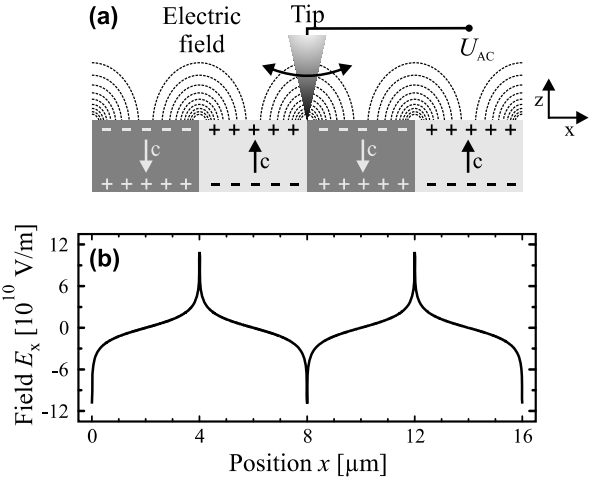

Fig. 8.10. (**a**) Schematic drawing of the static electric fields above the z face of a periodically poled ferroelectric crystal. Here c denotes the polar axis, U_{AC} the alternating voltage applied to the tip. (**b**) Electrical field component E_x 35 nm above the surface of a PPLN crystal with a period length of 8 µm calculated using (8.2)

8.6.1 Origin of the Lateral Signal

The (uncompensated) surface polarization charge density for $LiNbO_3$ is $\sigma = 0.71$ C/m^2 [46]. Figure 8.10 shows a sidewise sketch of a PPLN crystal. Because of the surface polarization charges, electric fields build up whose strength parallel to the surface is most at the domain boundaries. The electric field $E_x(x, z)$ with x being the axis parallel to the surface and perpendicular to the domain boundaries and z denoting the distance from the sample surface for an infinite PPLN structure is given by [45]

$$E_x(x,z) = \frac{\sigma}{4\pi\varepsilon_0} \ln\left[\prod_{n=-\infty}^{\infty} \frac{[(x+2na)^2+z^2]^2}{[(x+2na+a)^2+z^2]^2}\right] \tag{8.2}$$

with a denoting the domain size (PPLN period: $\Lambda = 2a$) and n the number of domains being included. For the PPLN sample investigated ($\Lambda = 8$ µm), electric field strengths of 10^{11} V/m are theoretically expected if no compensation of the surface charges is assumed.

8.6.2 Application to PPLN

In Fig. 8.11 the experimental results for deflection (a) and torsion (b) images of the end of a poled stripe of PPLN are shown with the corresponding scan lines in (d). The orientation of the cantilever was chosen to be parallel to the stripe (see also inset of Fig. 8.11(a, b)). At first sight it is obvious that the deflection image

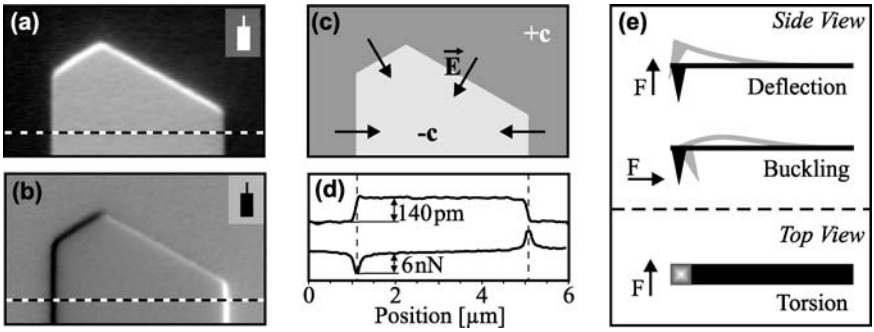

Fig. 8.11. Deflection (**a**) and torsion (**b**) images simultaneously recorded on a $LiNbO_3$ crystal (image size $6 \times 3.5\,\mu m^2$) with the corresponding scanlines (**d**) with 10 V_{pp} applied to the tip. The orientation of the chip with the cantilever is shown as *insets* in (**a**) and (**b**). Schematic drawing (**c**) of the electric field distribution **E**. In (**e**) the possible movements of the cantilever are depicted. The deflection image (**a**) shows deflection (PFM) and buckling (LEFM), the torsion image (**b**) the twisting of the cantilever (LEFM)

(a) shows the domain faces (due to the converse piezoelectric effect), whereas the torsion image (b) only shows the domain boundaries, at the left edge as a dark stripe and at the right edge as a bright stripe. The contrast inversion is due to the change of the direction of the electric field (see also Fig. 8.11(c)). The contrast is reduced when the electric field vector perpendicular to the cantilever becomes smaller as it can be seen on the tilted edges of the domain. As the cross-talk between vertical and lateral signals was suppressed [19], the level of the torsion signal within and outside the domain is same. Looking more closely at Fig. 8.11(a), at the top edges of the domain, a bright stripe is visible. When comparing with the schematic drawing of the electric field configuration in Fig. 8.11(c), at these edges, the electric field has a component along the axis of the cantilever. This also leads to lateral forces acting on the tip which result in a buckling of the cantilever. Quantitatively comparing the measured lateral forces with the ones expected from a simple model suggests a compensation of the surface polarisation charges by a factor of 100–1000. However, this is in full agreement with previously published data [47, 48].

To proof that electrostatic forces are responsible for the lateral signals at the domain boundaries, we performed comparative experiments with periodically poled $KTiOPO_4$ crystals. Because the piezoelectric coefficient d_{333} of $KTiOPO_4$ [49] is comparable to the one of $LiNbO_3$, the expected tilting of the surface at the domain boundaries should be identical. The measured lateral forces, however, are smaller by a factor of 2.6 with respect to those on $LiNbO_3$. This agrees with an electrostatic origin of the lateral forces as the surface polarization charge density is approximately three times smaller for $KTiOPO_4$ than for $LiNbO_3$ [40, 46].

8.7 Conclusions

Our aim in this chapter was to clear out inconsistencies and surprising features that were reported previously in connection with PFM measurements. In the end, it turns out, that the discovery of the system-inherent background leads to a simplification of the interpretation of the observed signals and enables to record quantitative data with PFM. All signals detected on the polar faces of multi-domain single crystals can be explained by the converse piezoelectric effect for the deflection (on top of the domain faces) and electrostatic interaction for torsion and buckling (at the domain boundaries).

References

1. M.M. Fejer, G.A. Magel, D.H. Jundt, R.L. Byer, Quasi-phase-matched 2nd harmonic-generation – tuning and tolerances. IEEE J. Quantum Electron. **28**, 2631–2654 (1992)
2. L.E. Myers, R.C. Eckardt, M.M. Fejer, R.L. Byer, Quasi-phase-matched optical parametric oscillators in bulk periodically poled $LiNbO_3$. J. Opt. Soc. Am. B **12**, 2102–2116 (1995)
3. H. Ishiwara, M. Okuyama, Y. Arimoto, *Ferroelectric Random Access Memories: Fundamentals and Applications*, vol. 93 (Springer, Berlin, 2004)
4. E. Soergel, Visualization of ferroelectric domains in bulk single crystals. Appl. Phys. B **81**, 729–752 (2005)
5. M. Alexe, A. Gruverman, *Nanoscale Characterisation of Ferroelectric Materials* (Springer, Berlin, 2004)
6. R.E. Newnham, *Properties of Materials: Anisotropy, Symmetrie, Structure* (Oxford University Press, Oxford, 2005)
7. J. Erhart, Domain wall orientations in ferroelastics and ferroelectrics. Phase Transitions **77**, 989–1074 (2004)
8. M.E. Lines, A.M. Glass, *Principles and Applications of Ferroelectrics and Related Materials* (Oxford University Press, New York, 2001)
9. B.A. Strukov, A.P. Levanyuk, *Ferroelectric Phenomena in Crystals* (Springer, Berlin, 1998)
10. J.A. Gonzalo, B. Jiménez (eds.), *Ferroelectricity: The Fundamentals Collection* (Wiley-VCH Verlag, Weinheim, 2005)
11. R.S. Weis, T.K. Gaylord, Lithium niobate: summary of physical properties and crystal structure. Appl. Phys. A **37**, 191–203 (1985)
12. J.C. Brice, *Crystal Growth Processes* (Halsted, New York, 1986)
13. J.F. Nye, *Physical Properties of Crystals* (Oxford University Press, Oxford, 1985)
14. V. Gopalan, T.E. Mitchell, Y. Furukawa, K. Kitamura, The role of nonstoichiometry in 180° domain switching of $LiNbO_3$ crystals. Appl. Phys. Lett. **72**, 1981–1983 (1998)
15. M.C. Wengler, B. Fassbender, E. Soergel, K. Buse, Impact of ultraviolet light on coercive field, poling dynamics and poling quality of various lithium niobate crystals from different sources. J. Appl. Phys. **96**, 2816–2820 (2004)
16. K.K. Wong, *Properties of Lithium Niobate* (INSPEC, London, 2002)
17. D. Sarid, *Scanning Force Microscopy* (Oxford University Press, London, 1994)
18. E. Soergel, W. Krieger, V.I. Vlad, Charge distribution on photorefractive crystals observed with an atomic force microscope. Appl. Phys. A **66**, S337–S340 (1998)

19. Á. Hoffmann, T. Jungk, E. Soergel, Cross-talk correction in atomic force microscopy. Rev. Sci. Instrum. **78**, 016101 (2007)
20. M. Reinstaedtler, U. Rabe, V. Scherer, J.A. Turner, W. Arnold, Imaging of flexural and torsional resonance modes of atomic force microscopy cantilevers using optical interferometry. Surf. Sci. **532–535**, 1152–1158 (2003)
21. S.V. Kalinin, A. Gruverman, *Scanning Probe Microscopy: Electrical and Electromechanical Phenomena at the Nanoscale* (Springer, Berlin, 2006)
22. T. Jungk, Á. Hoffmann, E. Soergel, Challenges for the determination of piezoelectric constants with piezoresponse force microscopy. Appl. Phys. Lett. **91**, 253511 (2007)
23. M. Labardi, V. Likodimos, M. Allegrini, Force-microscopy contrast mechanisms in ferroelectric domain imaging. Phys. Rev. B **61**, 14390–14398 (2000)
24. A. Agronin, M. Molotskii, Y. Rosenwaks, E. Strassburg, A. Boag, S. Mutchnik, G. Rosenman, Nanoscale piezoelectric coefficient measurements in ionic conducting ferroelectrics. J. Appl. Phys. **97**, 084312 (2005)
25. J.W. Hong, K.H. Noh, S. Park, S.I. Kwun, Z.G. Khim, Surface charge density and evolution of domain structure in triglycine sulfate determined by electrostatic-force microscopy. Phys. Rev. B **58**, 5078–5084 (1998)
26. M. Shvebelman, P. Urenski, R. Shikler, G. Rosenman, Y. Rosenwaks, M. Molotskii, Scanning probe microscopy of well-defined periodically poled ferroelectric domain structure. Appl. Phys. Lett. **80**, 1806–1808 (2002)
27. K. Takata, Comment on "Domain structure and polarization reversal in ferroelectrics studied by atomic force microscopy". J. Vac. Sci. Technol. B **14**, 3393–3394 (1996). [J. Vac. Sci. Technol. B **13**, 1095 (1995)]
28. H. Ogi, Y. Kawasaki, M. Hirao, H. Ledbetter, Acoustic spectroscopy of lithium niobate: elastic and piezoelectric coefficients. J. Appl. Phys. **92**, 2451–2456 (2002)
29. O. Kolosov, A. Gruverman, J. Hatano, K. Takahashi, H. Tokumoto, Nanoscale visualization and control of ferroelectric domains by atomic force microscopy. Phys. Rev. Lett. **74**, 4309–4312 (1995)
30. M. Labardi, V. Likodimos, M. Allegrini, Resonance modes of voltage-modulated scanning force microscopy. Appl. Phys. A **72**, S79–S85 (2001)
31. S. Hong, H. Shin, J. Woo, K. No, Effect of cantilever-sample interaction on piezoelectric force microscopy. Appl. Phys. Lett. **80**, 1453–1455 (2002)
32. C. Harnagea, M. Alexe, D. Hesse, A. Pignolet, Contact resonances in voltage-modulated force microscopy. Appl. Phys. Lett. **83**, 338–340 (2003)
33. C.H. Xu, C.H. Woo, S.Q. Shi, Y. Wang, Effects of frequencies of AC modulation voltage on piezoelectric-induced images using atomic force microscopy. Mater. Charact. **52**, 319–322 (2004)
34. S.V. Kalinin, D.A. Bonnell, Imaging mechanism of piezoresponse force microscopy of ferroelectric surfaces. Phys. Rev. B **65**, 125408 (2002)
35. L.M. Eng, H.-J. Güntherodt, G. Rosenman, A. Skliar, M. Oron, M. Katz, D. Eger, Nondestructive imaging and characterization of ferroelectric domains in periodically poled crystals. J. Appl. Phys. **83**, 5973–5977 (1998)
36. T. Jungk, Á. Hoffmann, E. Soergel, Quantitative analysis of ferroelectric domain imaging with piezoresponse force microscopy. Appl. Phys. Lett. **89**, 163507 (2006)
37. T. Jungk, A. Hoffmann, E. Soergel, Consequences of the background in piezoresponse force microscopy on the imaging of ferroelectric domain structures. J. Microsc. Oxford **227**, 76–82 (2007)
38. W. Heywang, H. Thomann, Tailoring of piezoelectric ceramics. Ann. Rev. Mater. Sci. **14**, 27–47 (1984)

39. T. Jungk, A. Hoffmann, E. Soergel, Influence of the inhomogeneous field at the tip on quantitative piezoresponse force microscopy. Appl. Phys. A **86**, 353–355 (2007)
40. G. Rosenman, A. Skliar, M. Oron, M. Katz, Polarization reversal in $KTiOPO_4$ crystals. J. Phys. D **30**, 277–282 (1997)
41. J. Padilla, W. Zhong, D. Vanderbilt, First-principles investigation of 180° domain walls in $BaTiO_3$. Phys. Rev. B **53**, R5969–R5973 (1996)
42. T. Jungk, A. Hoffmann, E. Soergel, Impact of the tip radius on the lateral resolution in piezoresponse force microscopy. New J. Phys. **10**, 013019 (2008)
43. D.A. Scrymgeour, V. Gopalan, Nanoscale piezoelectric response across a single antiparallel ferroelectric domain wall. Phys. Rev. B **72**, 024103 (2005)
44. J. Wittborn, C. Canalias, K.V. Rao, R. Clemens, H. Karlsson, F. Laurell, Nanoscale imaging of domains and domain walls in periodically poled ferroelectrics using atomic force microscopy. Appl. Phys. Lett. **80**, 1622–1624 (2002)
45. T. Jungk, A. Hoffmann, E. Soergel, Detection mechanism for ferroelectric domain boundaries with lateral force microscopy. Appl. Phys. Lett. **89**, 042901 (2006)
46. K.-H. Hellwege (ed.), *Landolt-Börnstein: Numerical Data and Functional Relationships in Science and Technology. New Series*, vol. III/16 (Springer, Berlin, 1981)
47. V. Likodimos, M. Labardi, M. Allegrini, N. Garcia, V.V. Osipov, Surface charge compensation and ferroelectric domain structure of triglycine sulfate revealed by voltage-modulated scanning force microscopy. Surf. Sci. **490**, 76–84 (2001)
48. S.V. Kalinin, D.A. Bonnell, Local potential and polarization screening on ferroelectric surfaces. Phys. Rev. B **63**, 125411 (2001)
49. H. Graafsma, G.W.J.C. Heunen, S. Dahaoui, A.El. Haouzi, N.K. Hansen, G. Marnier, The piezoelectric tensor element d_{33} of $KTiOPO_4$ determined by single crystal X-ray diffraction. Acta Crystallograph. B **53**, 565–567 (1997)